ACS APPLIED MATERIALS & INTERFACES

Research Article

Cite This: ACS Appl. Mater. Interfaces 2018, 10, 2515−2525

www.acsami.org

Spray-Drying-Induced Assembly of Skeleton-Structured SnO_2/Graphene Composite Spheres as Superior Anode Materials for High-Performance Lithium-Ion Batteries

Dongdong Liu,[†,#] Zhen Kong,[†,#] Xuehua Liu,[†] Aiping Fu,[†] Yiqian Wang,[‡] Yu-Guo Guo,[§] Peizhi Guo,[†] Hongliang Li,[*,†] and Xiu Song Zhao[†,∥]

[†]Institute of Materials for Energy and Environment, Laboratory of New Fiber Materials and Modern Textile, Growing Basis for State Key Laboratory, College of Materials Science and Engineering, Qingdao University, Qingdao 266071, China

[‡]College of Physics, Qingdao University, No. 308 Ningxia Road, Qingdao 266071, China

[§]Beijing National Laboratory for Molecular Sciences, Institute of Chemistry, Chinese Academy of Sciences (CAS), Beijing 100190, China

[∥]School of Chemical Engineering, The University of Queensland, St Lucia, Brisbane, Queensland 4072, Australia

Supporting Information

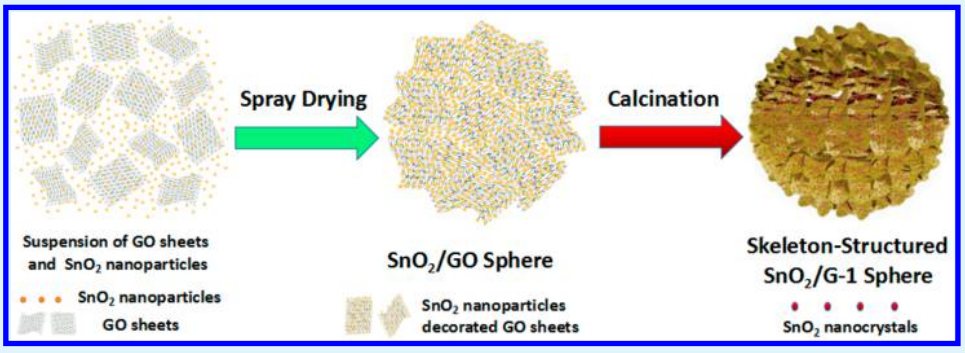

ABSTRACT: Three-dimensional skeleton-structured assemblies of graphene sheets decorated with SnO_2 nanocrystals are fabricated via a facile and large-scalable spray-drying-induced assembly process with commercial graphene oxide and SnO_2 sol as precursors. The influences of different parameters on the morphology, composition, structure, and electrochemical performances of the skeleton-structured SnO_2/graphene composite spheres are studied by XRD, TGA, SEM, TEM, Raman spectroscopy, and N_2 adsorption−desorption techniques. Electrochemical properties of the composite spheres as the anode electrode for lithium-ion batteries are evaluated. After 120 cycles under a current density of 100 mA g^{-1}, the skeleton-structured SnO_2/graphene spheres still display a specific discharge capacity of 1140 mAh g^{-1}. It is roughly 9.5 times larger than that of bare SnO_2 clusters. It could still retain a stable specific capacity of 775 mAh g^{-1} after 50 cycles under a high current density of 2000 mA g^{-1}, exhibiting extraordinary rate ability. The superconductivity of the graphene skeleton provides the pathway for electron transportation. The large pore volume deduced from the skeleton structure of the SnO_2/graphene composite spheres increases the penetration of electrolyte and the diffusion of lithium ions and also significantly enhances the structural integrity by acting as a mechanical buffer.

KEYWORDS: *tin dioxide, graphene, spray drying, skeleton structure, lithium-ion battery*

1. INTRODUCTION

Lithium-ion batteries (LIBs) are an ideal power supply for consumer electronics. They are also expected to play a prominent role as electrochemical storage systems in the development of sustainable energy as well as power systems for hybrid and electric vehicles.[1−3] However, the conventional graphite electrode that has been used as the anode for LIBs cannot fulfill the increasing demands for power sources with high energy density because of its low capacity of 372 $mAhg^{-1}$ in theory.[4−6] A growing concern is the acquisition of options of anode materials with low price, improved safety, high energy density, and durable cycle life.[7−9] Alloy or metal oxides have been regarded as promising anode materials for LIBs due to the superior energy capacity and impressive safety character.[10,11] As a kind of promising candidate anode for LIBs, tin dioxide (SnO_2) has attracted intensive attention owing to its low cost and high theoretical capacity of 782 mAh g^{-1}.[12−14] However, the relative low conductivity and especially the severe volume

Received: October 19, 2017
Accepted: December 22, 2017
Published: December 22, 2017

DOI: 10.1021/acsami.7b15916
ACS Appl. Mater. Interfaces 2018, 10, 2515−2525

variation of pristine SnO_2 particles during charging/discharging leads to serious mechanical disintegration (e.g., breaking and comminuting), destroying the conduction routes in the electrodes, which thus depresses the performance of the battery.[15−17] To tackle these problems, several endeavors are explored to enhance the electronic conductivity and the integrality of SnO_2-based electrodes.[18−20] Therein, the construction of a porous structure and the formation of carbon/metal (oxide) composites have been considered to be efficient strategies for improving the performance of alloy (or metal oxide) anode materials.[21,22] An electrode with three-dimensional (3D) porosity and abundant pores could counteract the volume distension of the active material.[23−25] Carbon/metal (oxide) composite materials have been shown to display improved electric and ionic conductivity, since the porous carbon materials play the role in buffering the volume change of the composite electrode.[26,27] It has been found that carbon-supported SnO_2 materials with a rationally designed structure and composition can improve Li-storage performance.[28,29] Various SnO_2 nanostructures, for example, nanotubes, hollow spheres, etc., are fabricated to improve the surface area and to shorten the diffusion path of Li^+, easing the interior strain induced due to the change of volume in the charging and discharging processes.[30−32] As for the composites, a great deal of efforts have been dedicated to finding appropriate carbon sources and facile approaches for the preparation of SnO_2/carbon composite electrodes.[33,34] Graphene has been found to be an appropriate carbon material for enhancing the properties of SnO_2.[35,36] Consequently, many endeavors have been performed to fabricate a composite of SnO_2 and graphene with a novel structure, and most of the resulted composites exhibited high energy density and superior reversible capacity.[37,38] In comparison with two-dimensional (2D) graphene nanosheets, 3D graphene architectures (e.g., graphene foams or skeletons) derived from 2D sheets can provide a higher specific surface area, flexible structure, and more voids for accommodating or encapsulating the SnO_2 nanoparticles, which can increase further the structural stability and the electrochemical performance of the SnO_2/graphene composite materials.[39−41] However, the formation of a 3D graphene assembly with a spherical morphology is still problematic since there is a lack of an efficient method to prepare them on the large scale, especially utilizing low-cost raw materials.

Herein, we depict a facile way to fabricate SnO_2/graphene composite spheres in which the graphene sheets are assembled into a skeleton-structured 3D spherical network. The mass-producible technique and industrial preparation method for powders, namely spray drying, was conveyed to the assembly of the skeleton-structured 3D SnO_2/graphene composite spheres by simply using $SnCl_4$ and commercial graphene oxide as precursors and combining with a calcination process. SnO_2/graphene composite spheres with superior capacity, extraordinary rate capability and excellent cycle persistence as anode materials for LIBs have been obtained through this spray-drying-assisted facile method. The effects of various preparation conditions of the 3D SnO_2/graphene composite spheres, especially the applied temperature for calcination, on their structure and performance as an LIB electrode were also systematically investigated, aiming at obtaining SnO_2/graphene composite spheres with high stability and excellent performance via flexible control of their structure and conformation.

2. EXPERIMENTAL SECTION

2.1. Materials. Tin(IV) chloride pentahydrate, ammonium hydroxide, and absolute ethanol are all of AR grade and utilized as purchased with no additional purification. Graphene oxide (GO) powder is received as a gift from the Sixth Element Ltd. (Changzhou) and used as obtained.

2.2. Preparation of the SnO_2/Graphene Composite Spheres. First, 0.25 g of graphene oxide was added to 100 mL of an ethanol and deionized water mixture (ethanol/deionized water = 3:7, v/v) followed by sonication for 2 h. Tin(IV) chloride pentahydrate (3.5 g) was dissolved in the above suspension under vigorous stirring at 60 °C. Ammonium hydroxide with a concentration of 0.5 mol/L was then exported into the suspension dropwise via a peristaltic pump (1 mL·min^{-1}) until the pH value of the suspension got to 3−5. Then, the obtained brownish black suspension was imported into the nozzle on a lab-scale SP-1500 spray dryer. The imported suspension is pulverized by the shear force from the pressurized air with a pressure in the range of 200−400 kPa, spraying out tiny droplets of SnO_2/GO suspension through the orifice of the nozzle. The liquid droplets quickly evaporated upon contact with the carrier gas of 160 °C hot air passing through the chamber of the dryer, resulting in dry and stable porous SnO_2/GO microspheres. Dried SnO_2/GO microspheres were collected finally by an online cyclone separator. The SnO_2/GO microspheres were calcined in nitrogen atmosphere at 550 or 650 °C, respectively, for 4 h to obtain samples SnO_2/G-1-550 and SnO_2/G-1-650, respectively, where 550 and 650 represent the calcination temperature.

As control experiments, pristine SnO_2 spheres were prepared with the same procedure as that for SnO_2/G-1 but using a suspension without graphene oxides. SnO_2/GO solid was also prepared by ordinary evaporation drying instead of spray drying, and then, the dried solid was calcined at 550 °C for 4 h under nitrogen atmosphere. The resulting sample is labeled as SnO_2/G-2-550.

2.3. Characterization. Phase recognition (XRD) of the samples was achieved by a Rigaku Ultima IV X-ray diffractometer using Cu Kα radiation (λ = 1.5418 Å). Fourier transform infrared (FTIR) spectra were acquired in the range of 400 to 4000 cm^{-1} on a Nicolet IS50 spectrophotometer. The morphology and the structure were examined on a JSM-7800 scanning electron microscope (SEM) and a JEM-2100 transmission electron microscope (TEM, JEOL Ltd.). Thermogravimetric analysis (Mettler Toledo TGA-2) was conducted in air atmosphere with a temperature ramp of 5 °C min^{-1}. X-ray photoelectron spectroscopy (XPS) data were recorded on a PHI VersaProbe III (ULVAC-PHI INC.) X-ray photoelectron spectrometer with a monochromatized Al K standard X-ray source. C 1s of 283.8 eV has been considered to be the internal standard to calibrate the binding energies. N_2 adsorption−desorption isotherms were recorded with an Autosorb-IQ-MP/XR surface area and pore analyzer (Quantachrome). Specific surface areas were calculated with the Brunauer−Emmett−Teller (BET) model using nitrogen adsorption data obtained in between P/P_0 = 0.05−0.35. The Barrett−Joyner−Halenda (BJH) model was utilized to determining the pore size distributions based on the desorption branch of the N_2 isotherms. A Renishaw inVia Plus Micro-Raman spectroscope was used to record the Raman spectra with a 532 nm excitation wavelength.

2.4. Electrochemical Measurements. The active materials (SnO_2/G), acetylene black, and polyvinylidene difluoride (PVDF) solution in *N*-methyl-2-pyrrolidine (NMP) were mixed with a weight ratio of 8:1:1. The slurry mixture was daubed onto a copper foil and then dried at 110 °C under vacuum for 12 h to evaporate water and NMP. Round electrodes with a size of 10 mm were cut out and weighed, and the precise loadings of the active materials were kept in a range of 1.46−1.66 mg/cm^2. A 1 M $LiPF_6$ solution in an EC/DEC/DMC mixture (1:1:1 in volume) was utilized as the electrolyte. Coin cells of 2016-type were then fixed in an Ar-filled glovebox (oxygen and moisture less than 1 ppm) using Celgard 2400 film as separator. Pristine lithium foil has been utilized as the counter electrode. The charge−discharge measurements were performed on a 2001A cell test system (LAND, Wuhan) with cutoff voltages between 3 and 0.01 V.

DOI: 10.1021/acsami.7b15916
ACS Appl. Mater. Interfaces 2018, 10, 2515−2525

Cyclic voltammetry (CV) studies with coin-type cells in a two-electrode configuration were carried out in the range of 0.01 to 3 V with a scan rate of 0.2 mV s^{-1} using a CHI760D electrochemical working station. Electrochemical impedance spectroscopy (EIS) surveys were collected with the same electrochemical working station in a frequency scope from 100 kHz to 0.01 Hz at an amplitude of 5 mV.

3. RESULTS AND DISCUSSION

3.1. XRD. The XRD curves of pristine SnO_2, SnO_2/G-1-550, and SnO_2/GO-1-650 samples along with a control sample of SnO_2/G-2 are shown in Figure 1. It can be seen that all samples exhibited four major diffraction peaks at 2θ = 26.7, 34.0, 38.2, and 66.0°, respectively. These peaks can be indexed to the (110), (101), (211), and (301) planes of SnO_2 in the tetragonal rutile phase (JCPDS No. 41−1445).[42] When the SnO_2/GO composite spheres were calcined at 650 °C in nitrogen atmosphere for 4 h, additional peaks at 2θ = 26.7, 34.0, 38.2, and 66.0° appear. These peaks can be ascribed to the typical planes of (200), (101), (220), and (211) of metallic Sn (JCPDS No. 86−2265),[43] demonstrating that a large proportion of SnO_2 had been reduced to metallic Sn under such calcination conditions. From the XRD pattern of SnO_2/G-2-550, it can be seen that the control sample showed much weaker characteristic peaks of SnO_2 in comparison with that of SnO_2/G-1-550, indicating the amorphous nature of the SnO_2 particles. The discrepancy of the crystallinity for SnO_2 nanoparticles in SnO_2/G-1-550 and SnO_2/G-2-550 can be explained due to the surface effect and the wrapping effect, which can alter somehow the phase transition temperature. Similar phenomena have also been observed for TiO_2 nanoparticles due to their condensed contact or to the wrapping of the particles with other kinds of compounds.[44,45] Such a speculation has been verified by the following morphology and porosity investigation. No characteristic peaks for graphene can be detected in these SnO_2/G composites, revealing a disordered stacking of the graphene sheets.[46] To get more information on the SnO_2 particles, the Debye−Scherrer equation, $L = 0.89\lambda/B\cos\theta$, was exploited to evaluate the size of the SnO_2 particles, where L is the mean size of SnO_2 nanoparticles, B represents the FWHM (full-width at half-maximum) of the applied peak in radians, λ denotes the

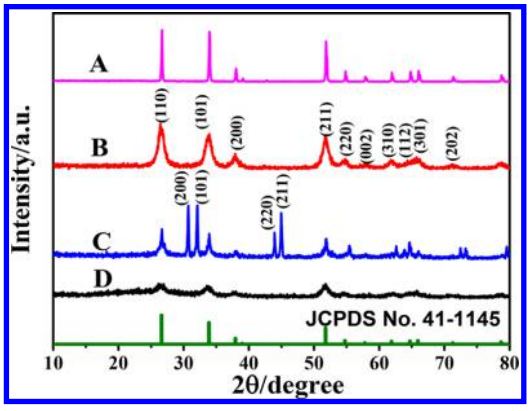

Figure 1. XRD curves of the bare SnO_2 control sample (curve A), SnO_2/G-1-550 (curve B), SnO_2/G-1-650 (curve C), and the control sample of SnO_2/G-2-550 (curve D), and the standard JCPDS pattern of SnO_2 with tetragonal rutile phase.

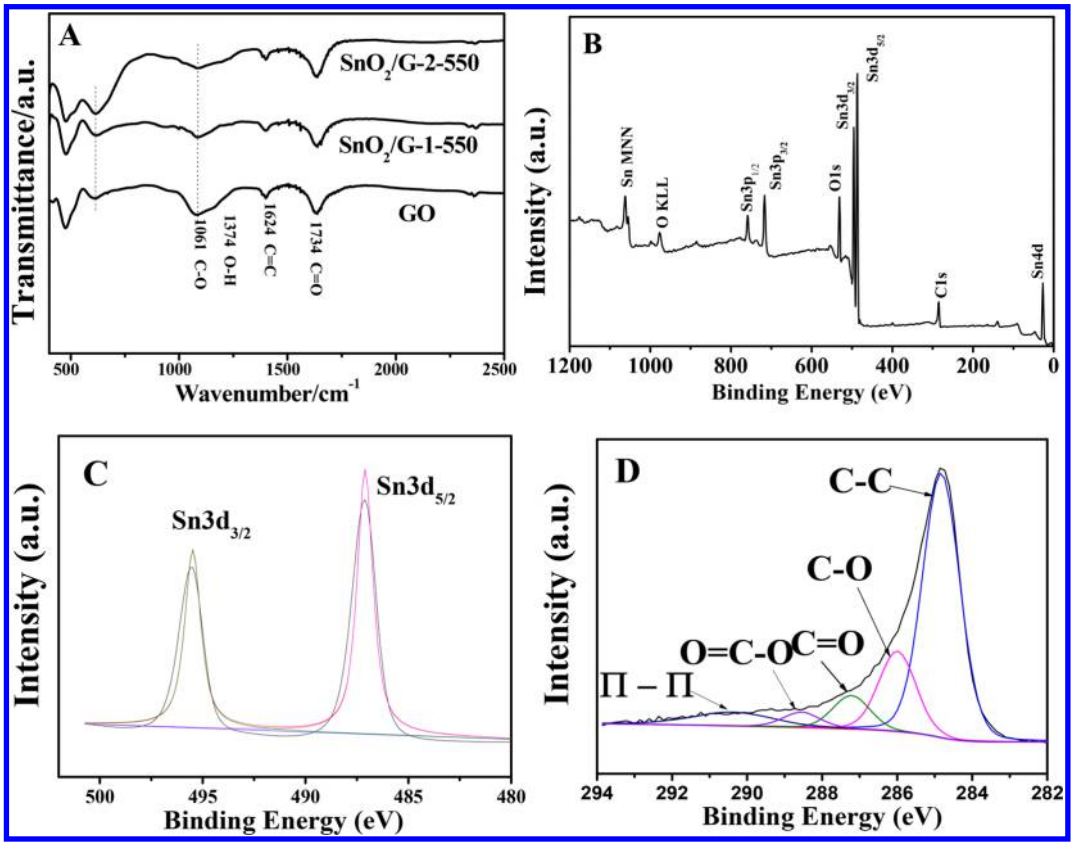

Figure 2. FTIR spectra of the graphene oxide raw material and those of the SnO_2/G-1-550 and SnO_2/G-2-550 composites (A). The XPS full survey of SnO_2/G-1-550 (B), and high-resolution XPS surveys of Sn 3d (C) and C 1s (D) regions.

DOI: 10.1021/acsami.7b15916
ACS Appl. Mater. Interfaces 2018, 10, 2515−2525

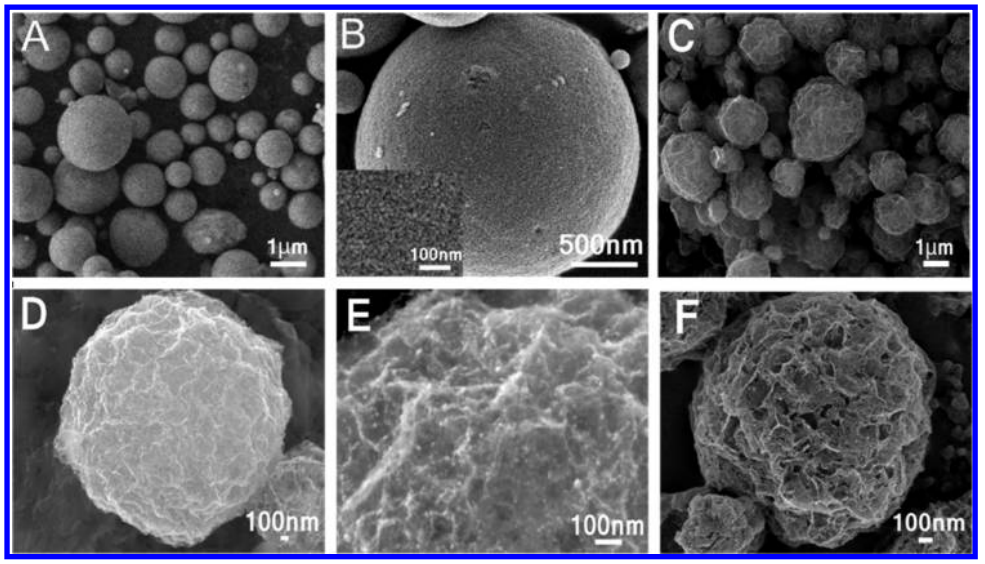

Figure 3. SEM images of the pristine SnO_2 spheres (A,B), SnO_2/G-1-550 composite spheres with different magnifications (C−E), and an individual SnO_2/G-1-550 composite sphere with obvious skeleton structure (F).

wavelength of the selected X-ray radiation, and θ corresponds to the diffraction angle.[47] L values of about 9.0 and 6.5 nm for SnO_2 nanocrystals in pristine SnO_2 microspheres and SnO_2/G-1-550, respectively, have been deduced based on the (110) peak of their XRD patterns.

3.2. FTIR Spectra and XPS Measurements. Panel A in Figure 2 shows the FTIR spectra of the GO precursor, SnO_2/G-1-550, and SnO_2/G-2-550 samples recorded in a wavelength ranging from 400 to 2500 cm^{-1}. Several peaks around 1734, 1374, 1061, and 1624 cm^{-1} have been observed in the FTIR curve of GO, which can be ascribed to the stretching vibration of the C=O bond in carboxyl or carbonyl groups, the O−H in a carboxyl group or water, the C−O in epoxy or alkoxy groups, and also the vibration of C=C bonds in the unoxidized graphitic skeleton.[48] In these FTIR spectra of the SnO_2/G-1-550 and SnO_2/G-2-550 composites, the typical peaks for C−O, O−H, and C=O bonds turn obviously to being weaker in contrast to that of the C=C band, revealing the diminishing of most oxygen-related groups after calcination. The band centered at about 621 cm^{-1} turns to more visible in the patterns of SnO_2/G-1-550 and SnO_2/G-2-550. This peak can be attributed to the vibration of the Sn−O−Sn moiety, thus its growth demonstrates the existence of SnO_2 in the composite.[36]

The formation of SnO_2 has been confirmed further by XPS measurements. The XPS full survey and the high-resolution survey at the Sn 3d and C 1s regions have been presented as panels B to D in Figure 2. The full survey shows obviously the presence of Sn, C, and O elements. The peaks at 495.5 and 487.0 eV in the high-resolution XPS survey of Sn 3d can be designated as the characteristic signals of Sn $3d_{3/2}$ and Sn $3d_{5/2}$ for Sn (IV), confirming the existence of SnO_2 in the SnO_2/G-1-550 composite. The C 1s peak can be further deconvoluted into four peaks located at 284.8, 286.2, 287.6, and 289.1 eV (panel D), which could be assigned to C−C, C−O, C=O, and O−C=O groups, respectively.[24] A $\pi-\pi$-related peak at 290.6 eV is observed as well in SnO_2/G-1-550, indicating that the affinity between SnO_2 and graphene is strong. These XPS results are in good agreement with the FTIR results and demonstrate further that the SnO_2/G-1-550 composite consists of graphene and SnO_2 crystals.

3.3. SEM and TEM Investigations. The morphologies of pristine SnO_2 spheres and SnO_2/G-x (x = 1 or 2) were investigated using SEM, and the corresponding images are shown in Figure 3. From the images, it can be seen that pristine SnO_2 samples show a spherical morphology with smooth surface character and a sphere diameter of about 0.5−2 μm (image A). High-resolution SEM demonstrates that the spheres of pristine SnO_2 consist of nanoparticles with a size of about several nanometers, and the SnO_2 nanoparticles aggregated into a large-sized spherical cluster (see Image B and the inset therein). Amazingly, the SnO_2/G-1-550 composite sample consisted of SnO_2 nanoparticles and graphene sheets assembled also into a spherical morphology (image C). However, the SnO_2/G-1-550 composite spheres present a rough and wrinkled surface, which is completely distinct from that of the pristine SnO_2 spheres. The high-magnification SEM images show that the wrinkled morphology of the SnO_2/G-1-550 composite spheres originates mainly from the protuberant graphene sheets (see image D and E). A more close observation reveals that the graphene sheets connected loosely with each other and mostly were oriented to the sphere center, forming a novel skeleton-structured sphere (see image F and the inset therein, which show obvious skeleton character). The same images reveal also that SnO_2 particles with a size of several nanometers have been deposited tightly onto the surface of wrinkled graphene sheets. The SEM image of the skeleton-structured SnO_2/G-1-550 composite spheres show the existence of abundant void volume (see images D and F), and such a structure character will result in a high specific surface area and provide spaces for the volume expansion of SnO_2 particles during the alloying process with lithium[26] (section 3.7). Such a kind of structure is responsible for the superior electrochemical properties of the composite spheres (see section 3.8). EDS elemental mapping analysis has been performed over a selected area of one SEM image to detect the elements and their dispersion in the SnO_2/G-1-550 composite, and the results have been depicted in Figure S1 . Picture A of Figure S1 shows the overlap triple-elemental mapping of tin, oxygen, and carbon in the SnO_2/G-1-550 sample. Obviously, the high contrast of tin and oxygen signals in the overlap mapping suggest that the surface of the SnO_2/G-1-550 spheres

DOI: 10.1021/acsami.7b15916
ACS Appl. Mater. Interfaces 2018, 10, 2515−2525

was covered mainly with tin and oxygen. The individual elemental mapping of tin, oxygen, and carbon demonstrates the uniform dispersion of the SnO_2 nanocrystals and the graphene sheets, which confirm further the above observation by SEM and will be verified by TEM measurements as following. For comparison, SEM images of SnO_2/G-1-650 and SnO_2/G-2-550 are presented in Figure S2. From the images, it can be seen that SnO_2/G-1-650 also possesses a spherical morphology, albeit, with metallic Sn particles anchored onto the surface of the spheres (see the bright spots in image A of Figure S2). Differently, from the image of SnO_2/G-2-550, one can see only a bulk without any regular morphology, which demonstrates that spray drying plays an essential role in the formation of the SnO_2/G-1 spheres.

TEM measurements are performed to reveal further the detailed structure of SnO_2/G-1-550 composite spheres, and also the size and crystallinity of the enclosed SnO_2 particle therein. Picture A of Figure 4 shows the overview of an individual SnO_2/G-1-550 sphere. From the image, one can see clearly the porous property of the sphere. We can also see roughly the arrangements of the graphene sheets. The high-magnification TEM image of the same sphere shows that the SnO_2 particles with size of a few nanometers were dispersed homogeneously and anchored tightly onto the graphene layers, and a few of the particles were wrapped incompletely with graphene layers (image B). The size of the SnO_2 nanocrystals observed with TEM is close to the value derived from the Scherrer formula (see section 3.1). The TEM image predicts also that such a skeleton structure seems also favorable for preventing the aggregation of SnO_2 particles. From the high-resolution TEM image, one can see the very observable lattice fringes in a single SnO_2 nanocrystal (image C of Figure 4), and a plane spacing of about 0.34 nm, close to the spacing of the (101) facet of tetragonal rutile SnO_2 crystal, has been derived.[49] A selected area electron diffraction (SAED) pattern corresponding to these SnO_2 nanocrystals has been detected (Figure 4D). Obviously, the SAED pattern demonstrates well-defined rings consisting of bright spots, and they can be assigned to the (110), (101), (210), (211), and (112) facets of the SnO_2 crystal with a tetragonal rutile structure. Such a SAED pattern is in accordance with their XRD characteristic. To have a deeper insight into the composition, TEM measurements have also been carried out for the SnO_2/G-1-650 composite, and the results have been displayed in Figure S3. Panel A in Figure S3 is the overview TEM image of the SnO_2/G-1-650 sample, which shows clearly the decoration of the graphene sheets with some nanoparticles. The high-resolution TEM images B and C presented in Figure S3 display clearly lattice fringes with spacings of 0.33 and 0.288 nm, respectively, which can be indexed to the (110) and (200) lattice planes of SnO_2 and metallic Sn, correspondingly. The TEM observations are consistent with the XRD results, which prove that a part of the SnO_2 nanoparticles had been reduced to Sn during the high-temperature calcination process.

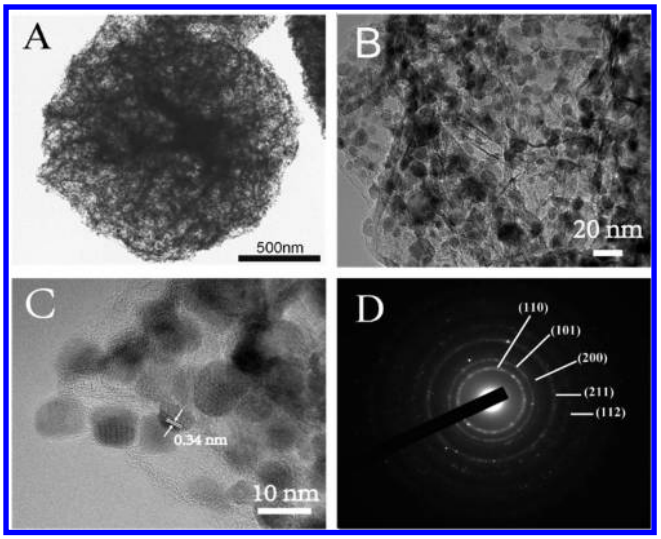

Figure 4. TEM images of the SnO_2/G-1-550 composite spheres (images A–C) with different magnifications, and selected area electron diffraction (SAED) pattern corresponding to these SnO_2 nanoparticles (image D).

3.4. Formation Mechanism of the Skeleton-Structured Composite Spheres. Based on the morphology and structure studies and the virtue of spray drying, a spray-drying-induced formation process of the skeleton-structured SnO_2/G-1-550 composite spheres has proposed and been illustrated in Scheme 1. First, commercial muddy GO stacks were dispersed into a water/ethanol mixture solvent, and then, the GO sheets were further peeled off from each other upon the ultrasound irradiation. After the mixing of the GO suspension with tin(IV) chloride and the subsequent addition of aqueous ammonia, amorphous SnO_2 nanoparticles were deduced via a sol–gel process. Meanwhile, a part of the formed SnO_2 nanoparticles were deposited in situ to the surface of GO sheets due to the presence of abundant functional groups therein. Then, a suspension containing colloidal SnO_2 nanoparticles and GO sheets decorated with SnO_2 nanoparticles were obtained. When

Scheme 1. Schematic Drawing for the Spray-Drying-Induced Formation of the SnO_2/G-1 Composite Sphere

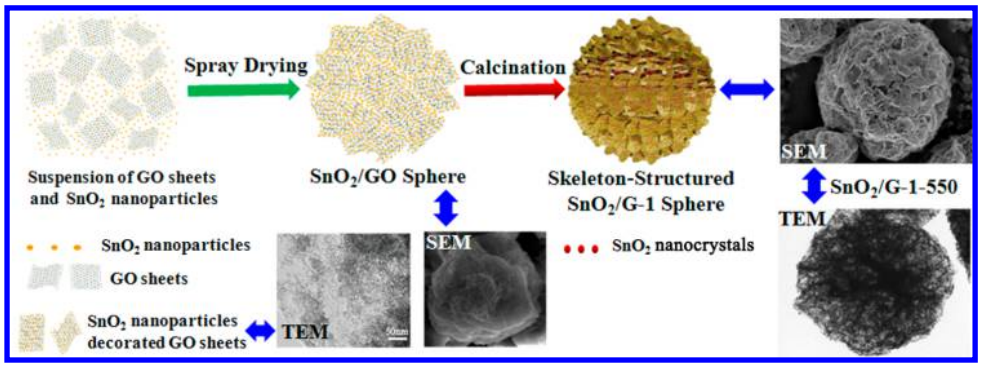

DOI: 10.1021/acsami.7b15916
ACS Appl. Mater. Interfaces 2018, 10, 2515–2525

the suspension was transported into the inlet of the spray dryer, they were pulverized upon the contact with pressurized air, spurting out numerous microdroplets of SnO_2/GO suspension through the nozzle orifice. The solvent in the microdroplets then evaporated transiently when the microdroplets were blew by the 160 °C hot air flow in a chamber of the dryer, resulting in dry and stable porous SnO_2/GO microspheres.[50]

The evaporation of solvent (water/ethanol mixture) results in the solidification of the suspension microdroplets. Meanwhile, the evacuation of the solvent steam from the interior of the microdroplets will produce an impact force to the GO layers, inducing the erection of the GO layers and finally resulting in the dried SnO_2/GO composite spheres with a skeleton structure and abundant pores. Dried SnO_2/GO microspheres were then collected by an online cyclone separator. After the calcination process in a nitrogen atmosphere at 550 or 650 °C for 4 h, crystallized SnO_2/G-1-550 and SnO_2/G-1-650 samples were acquired, respectively. As for the SnO_2/G-2 sample, it was solidified via an ordinary evaporation process instead of the spray drying as applied to SnO_2/G-1. In the normal evaporation process, SnO_2-decorated graphene sheets aggregated gradually and formed the agglomeration without a typical morphology. After calcinations in a nitrogen atmosphere at 550 °C for 4 h, SnO_2/G-2-550 with a bulk shape was acquired.

3.5. Thermal Analysis. To acquire the precious percentage of SnO_2 in the as-prepared sample, TGA analysis was performed in air at a temperature range between room temperature and 800 °C with a temperature ramp of 5 °C·min^{-1}. As shown in the TGA curve (Figure 5), the weight loss

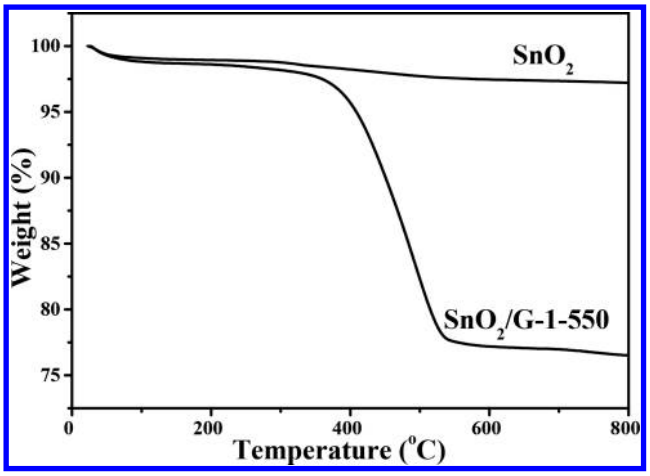

Figure 5. TGA curves of the pristine SnO_2 and the SnO_2/G-1-550 composite spheres.

below 100 °C in both of the curves could be attributed to the evaporation of adsorbed moisture. The pristine SnO_2 spheres exhibit a smooth weight loss in between room temperature and 800 °C with a total loss of about 2.80 wt %. For the SnO_2/G-1-550 composite spheres, a significant weight loss with a value of about 20 wt % took place from 350 to 550 °C, which is ascribed to the burning of carbon by oxygen.[27] The total loss of the composite up to 800 °C reach to about 76.5 wt %. Therefore, a mass percentage of about 78 wt % for SnO_2 in the SnO_2/G-1-550 series of composite spheres can roughly be deduced. For comparison, the content of SnO_2 in SnO_2/G-2-550 has been investigated by TGA as well, and the result has been depicted in Figure S4. From the curve, it can be seen that SnO_2/G-2-550 shows a weight loss of about 7.0% in between room temperature and 800 °C due mainly to the burning of carbon materials. Thus, the weight content of about 93 wt % for SnO_2 in the SnO_2/G-2-550 composite can be deduced. The difference of SnO_2 contents in SnO_2/G-1-550 and SnO_2/G-2-550 can be attributed to the drying techniques applied to them. The spray drying may result in a partial loss of the ultralight nanoparticles under a strong high-temperature air flow.

3.6. Raman Spectra. Raman spectroscopy is a powerful tool to identify ordering and disordering on the structure of carbon materials. As depicted in Figure 6, a G band at 1597

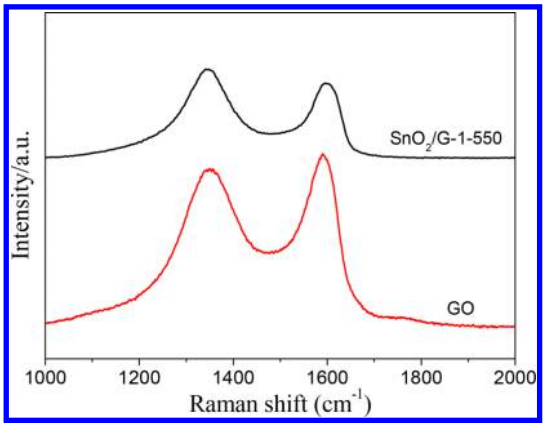

Figure 6. Raman spectra of the GO raw material and the SnO_2/G-1-550 sample.

cm^{-1} corresponding to the sp^2 hybridized carbon and another peak around 1346 cm^{-1} named as a D band deriving from the disordering of the carbon structure have been observed.[51] The disordering, normally caused by amorphizing of graphite, is believed to induce an growth of the ratio between the relative intensities of the D to G bands (I_D/I_G) due to the reduction of the sp^2 domain size. Evidently, the I_D/I_G value of SnO_2/G-1-550 (1.20) is much higher than that of GO (1.05), which can be explained as due to the intercalation of SnO_2 particles between the graphene layers or the anchor of the SnO_2 particles on the surface of the graphene layers in these SnO_2/G-1-550 composite spheres.

3.7. Nitrogen Adsorption−Desorption Results. N_2 adsorption−desorption has been employed to investigate the surface area and porosity of pristine SnO_2 spheres as well as SnO_2/G-1-550 and SnO_2/G-2-550 composites. Their isotherms and pore size distribution graphs are depicted in Figure 7A−C, respectively. All these samples show isothermal curves of type IV and display an apparent capillary condensation slope.

Obviously, adsorption−desorption hysteresis loops can also be observed in these isotherms. According to the IUPAC classification, the SnO_2/G-1-550 composite shows a hysteresis loop of type H3, while a type H2 hysteresis loop appears on the sorption isotherm of SnO_2/G-2-550. It is different from these composites, whereas the bare SnO_2 sample exhibited a slender and atypical hysteresis loop. Meanwhile, the stage of the capillary condensation shifted to a higher relative pressure, indicating that the porosity of the bare SnO_2 sphere is poorer than that of the composite samples.[52] The differences between the types of hysteresis loops among these samples can be due to the discrepancy of the arrangements or structures of the pores in them. Nevertheless, all these loops indicate the materials are abundant in mesopores.[53] The average pore sizes

DOI: 10.1021/acsami.7b15916
ACS Appl. Mater. Interfaces 2018, 10, 2515−2525

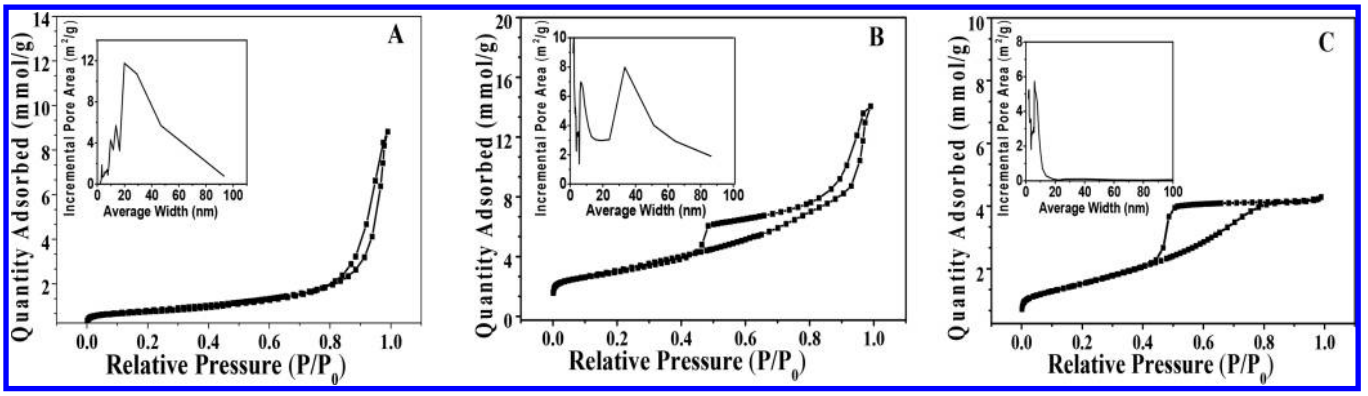

Figure 7. N_2 adsorption−desorption isotherms and pore size distribution graphs (inset) of pristine SnO_2 (panel A), SnO_2/G-1-550 (panel B), and SnO_2/G-2-550 (panel C).

of about 20, 35, and 6.5 nm for the pristine SnO_2 spheres as well as the SnO_2/G-1-550 and SnO_2/G-2-550 composites, respectively, were deduced. Impressively, obvious bimodal peaks for both the SnO_2/G-1-550 and SnO_2/G-2-550 samples can be observed. In addition to the large pore size (at about 35 nm) produced by the evaporation of solvent during the spray drying process, another kind of pore with a size of about 6.5 nm has also been detected in the SnO_2/G-1-550 composite. The small-sized mesopores in the SnO_2/G-1-550 spheres may originate from the stacking of graphene intercalated with SnO_2 nanoparticles. The SnO_2/G-2-550 sample shows a bimodal pore size distribution at about 2.3 and 6.5 nm, respectively, which are smaller than those in SnO_2/G-1-550 sample. The difference of the pore size between these two samples can be attributed to the applied drying technique, e.g., the ordinary drying process can induce more compact solid than that derived from spray drying. The detailed data of specific surface area and pore volume for pristine SnO_2 spheres, SnO_2/G-1-550, and SnO_2/G-2-550 samples are displayed in Table 1.

Table 1. BET Specific Surface Area and Pore Volume of Pristine SnO_2 Spheres, SnO_2/G-1-550, and SnO_2/G-2-550 Composites

	pristine SnO_2	SnO_2/G-1-550	SnO_2/G-2-550
surface area ($m^2\ g^{-1}$)	40	245	124
pore volume ($cm^3\ g^{-1}$)	0.03	0.41	0.15

The BET specific surface area and pore volume with values of 40 $m^2\ g^{-1}$ and 0.03 $cm^3\ g^{-1}$ for the bare SnO_2 spheres, 245 $m^2\ g^{-1}$ and 0.41 $cm^3\ g^{-1}$ for SnO_2/G-1-550 composite spheres, and 124 $m^2\ g^{-1}$ and 0.15 $cm^3\ g^{-1}$ for SnO_2/G-2-550 composite, respectively, were deduced. The large specific surface area of the SnO_2/G-1-550 composite spheres can be attributed to the formation of the skeleton-structured graphene spheres and the anchoring of nanosized SnO_2 particles on the graphene layers. The large pores, high specific surface area, and abundant pore space in SnO_2/G-1-550 sample can relieve the volume change of SnO_2 that occurred in the Li^+ insertion/desertion process, resulting in an excellent electrochemical performance. The N_2 adsorption−desorption measurements are consistent with the aforementioned SEM observations.

3.8. Electrochemical Properties. The electrochemical performance of the synthesized SnO_2/G-1-550 composite and SnO_2/G-2-550 are studied as active materials for the anodes of LIBs. A galvanostatic technique is used for the investigation of cycling performance for these composite anodes under a current density of 100 mA g^{-1}. Figure 8 shows the specific capacities and cycle performances of pristine SnO_2 (panel A), SnO_2/G-1-550 (panel B), and SnO_2/G-2-550 (panel C) composites. The reversible capacity of pristine SnO_2 fades obviously and shows a weak capacity of just 121 $mAhg^{-1}$ after 50 rounds (Figure 8A). With respect to the SnO_2/G composite spheres of different structures, charge capacities of about 1140 $mAhg^{-1}$ for SnO_2/G-1-550 (panels B) were retained after 120 charge−discharge cycles and 293 mAh g^{-1} was delivered for SnO_2/G-2-550 (panels C) after only 50 charge−discharge cycles, respectively. Obviously, the skeleton-structured composite spheres of SnO_2/G-1-550 exhibit much better cycle performances in comparison with the clusters of pristine SnO_2 spheres and the SnO_2/G-2-550 composites. The potential application of the SnO_2/G-1-550 composite has been explored by performing a long cycle test with a current density of 200 mA g^{-1}. After 200 cycles, a discharge capacity of about 680 $mAhg^{-1}$ could still be delivered by this promising material (Figure S5). However, the SnO_2/G-1-550 electrode also undergoes perceptible capacity decay after 110 cycles. Normally, the decline of capacity can be ascribed to the structure variation of the active materials and also to the decomposition of electrolyte and the increase of the SEI film. A deep insight of the structure evolution and the changes of the electrolyte and the solid electrolyte interface (SEI) film upon cycling requires a more advanced technique e.g., in situ TEM observation and in situ FTIR monitoring during the cycles, which will be the next endeavors of our study to this novel materials. Figure 8D presents the multirate capabilities of the SnO_2/G-1-550 sample measured at current densities in between 100 and 2000 mAg^{-1}. Although the capacities decreased with the increasing of the applied current density, the SnO_2/G-1-550 composite spheres still show superior reversible capacities. Under a current density of 100 mAg^{-1}, the discharge capacity remain at 1107 mAh g^{-1} after 10 cycles. At the 20th round with a current density of 200 mA g^{-1}, it could still reserve a discharge capacity of 1074 $mAhg^{-1}$. After an additional 10 cycles at a current density of 500 mA g^{-1}, the composite delivers a reversible capacity of 986 mAh g^{-1}. Even though under a large charge rate of 2000 mA g^{-1}, the composite still holds a satisfied reversible capacity of 775 mAh g^{-1} at the 50th cycle. Impressively, when the charging/discharging rate is restored to 100 mAg^{-1}, the specific capacity of the anode with the skeleton-structured SnO_2/G-1-550 composite can almost resume the original capacity and

DOI: 10.1021/acsami.7b15916
ACS Appl. Mater. Interfaces 2018, 10, 2515−2525

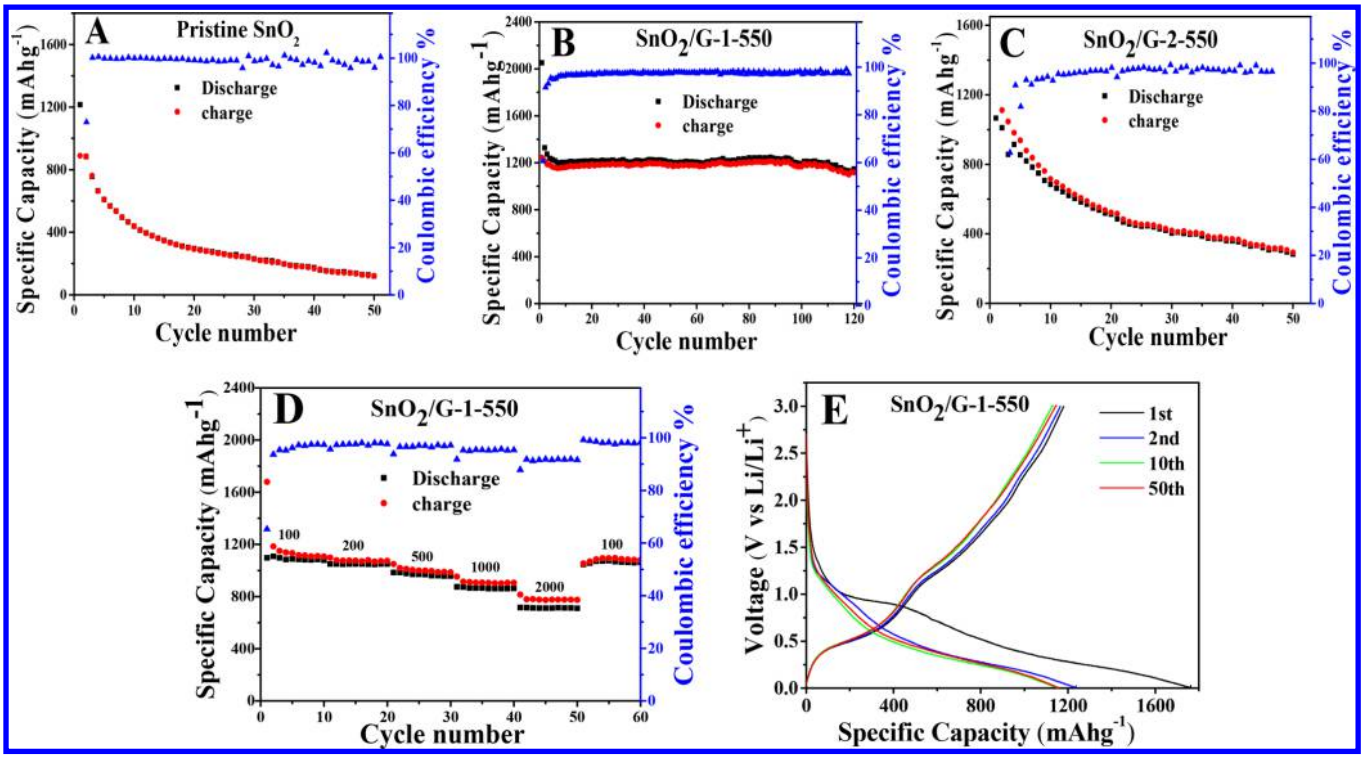

Figure 8. Cycling performance and Coulombic efficiency of different samples with a current density of 100 mAg^{-1}, pristine SnO_2 (panel A), SnO_2/G-1-550 (panel B), SnO_2/G-2-550 (panel C), Multirate capabilities of SnO_2/G-1-550 composite at currents between 100−2000 mA g^{-1} (panel D), and the first, second, 10th and 50th cycle charge−discharge curves at the current of 100 mA g^{-1} for the SnO_2/G-1-550 composite (panel E).

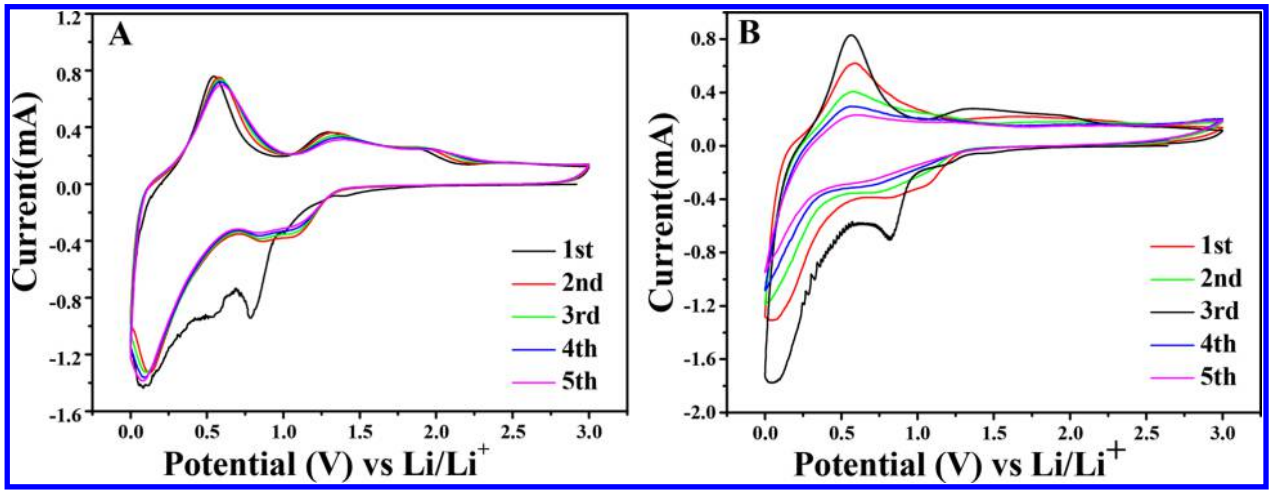

Figure 9. Cyclic voltammograms of the initial five scans in a voltage range of 0.01−3.0 V for SnO_2/G-1-550 (panel A) and SnO_2/G-2-550 (panel B) composites.

maintains a capacity of 1081 mAh g^{-1} at the 60th cycle. The restorability of the capacity to the original one when the charge rate went back demonstrates the outstanding reversibility of the composite used as anode and also reveals its potential application for high-rate LIBs. We suppose that the unique skeleton arrangement of the graphene sheets, the small size of SnO_2, and the large specific surface area are beneficial to the rate capability and cycling performance of the SnO_2/G-1 composites.[42] Figure 8E shows profiles for the voltage versus capacity at the 1st, 2nd, 10th, and 50th cycles for the SnO_2/G-1-550 composite anode in between voltages of 0.01 and 3.0 V at a current density of 100 mA g^{-1}. The profiles are close to the documented results, implying a similar electrochemical mechanism.[53,54] The as-fabricated SnO_2/G-1-550 composite shows a discharge capacity of 1762 mAh g^{-1} and a charge capacity of 1201 mAh g^{-1} for the first cycle, giving out an initial Coulombic efficiency of 68%. The irreversible capacity for the SnO_2/G-1-550 composite in the initial cycle could be due mostly to the formation of Li_2O and the decomposition of electrolyte on the surface of active materials and the deposition of a passivative SEI film therein, and also to some irreversible reaction for Sn and graphene during Li^+ insertion and extraction.[39] After the first cycle, the reversibility of the charge/discharge processes has been enhanced markedly. During the second cycle, the SnO_2/G-1-550 composite delivers a discharge capacity of 1237 mAh g^{-1} and a charge capacity of

DOI: 10.1021/acsami.7b15916
ACS Appl. Mater. Interfaces 2018, 10, 2515−2525

1180 mAh g^{-1}, deducing a Coulombic efficiency of 95%. From then on, the fading of capacity becomes weak and no obvious irreversible actions can be observed, suggesting that the irreversible actions took place principally in the initial cycle. Ten cycles later, a discharge capacity of 1151 mAh g^{-1} is obtained and a charge capacity of 1127 mAh g^{-1} can be reserved. The SnO_2/G-1-550 composite provide still a discharge capacity of 1154 mAh g^{-1} and a charge capacity of 1136 mAh g^{-1} at a current density of 100 mA g^{-1} even after 50 discharge−charge cycles. In comparison with documented tin oxide/graphene composites, the novel skeleton-structured SnO_2/G-1-550 composite spheres show also superior lithium storage properties.[55] A performance comparison of SnO_2/G-1-550 sample with other documented SnO_2-based composites as anode materials for Li ion batteries are summarized in Table S1.[56−58] It can be seen from the table that both the cycling ability and the capacity of SnO_2/G-1-550 composite is more prominent than those of most of the reported counterparts. The extraordinary rate stability of the electrode made of SnO_2/G-1-550 can be ascribed in the one hand to the integration of graphene sheets into the composite and on the other hand to the novel skeleton structure.[6] The former character will improve the conductivity of the composite while the latter property can alleviate the structure instability induced by volume variation of SnO_2. To verify this speculation, ex situ SEM and TEM measurements have been performed to the cycled electrode materials, and the results have been depicted in Figure S6. Panels A and B of Figure S6 shows the SEM and TEM images, respectively, of the active materials after 50 cycles at a current density of 200 mA/g. It can be seen that the morphologies of the SnO_2/G-1-550 composite spheres could remain roughly spherical (Figure S6A), and the SnO_2 nanoparticles still anchored tightly on the surface of the graphene substrates (Figure S6B), suggesting the structural integrity of the SnO_2/G-1-550 composite upon cycles.

To recognize the reactions in different cycles, CV of SnO_2/G-1-550 and SnO_2/G-2-550 composite electrodes were characterized with a voltage in between 0.01−3 V under a scan rate of 0.2 mVs^{-1}. Panel A of Figure 9 shows the CV profiles of SnO_2/G-1-550 in the first five scanning cycles. As shown in the profiles, two reduction peaks at 0.78 and 0.09 V are detected in the first cathodic scan, which is accordance with those reported results.[59] The former peak can be ascribed to the conversion of $SnO_2 + Li^+$ to $Sn + Li_2O$ as described in eq 2 and the establishing of a SEI film as indicated with eq 1. These processes are normally considered as irreversible and will result in evident capacity loss of the first cycle. The latter one of the two peaks in the first catholic process can be ascribed to the formation of Li_xSn alloys as depicted by eq 3.[60]

$$Li^+ + e^- + \text{electrolyte} \rightarrow \text{SEI (Li)} \quad (1)$$

$$SnO_2 + 4Li^+ + 4e^- \rightarrow Sn + 2Li_2O \quad (2)$$

$$Sn + xLi^+ + e^- \rightarrow Li_xSn\ (0 < x < 4.4) \quad (3)$$

In the first anodic sweep, one oxidization peak located around 0.55 V could be assigned to the alloying/dealloying processes as depicted by eq 3, which has been regarded as extremely reversible and has mainly contributed to the reversible capacities. For the second round scan, both of the two cathodic peaks switch to higher voltages, while the peak current decreased obviously, indicating the occurring of irreversible action in the first cathodic sweep. The CV graphs of the SnO_2/G-1-550 electrode become stable in between the following four cycles (from the second to the fifth cycle), and the following cycles are almost superimposed, implying a superior cyclability of this composite electrode. As shown in Figure 9B, the intensity of peak and integrated areas of these CV graphs in the first five round of scans reduced evidently for SnO_2/G-2-550 composite, indicating poor cycling stability. The result is consistent fairly with the cycling performance of charge/discharge processes under a constant current.

The Nyquist profiles of the electrochemical impedance spectroscopy (EIS) for pristine SnO_2, SnO_2/G-1-550, and SnO_2/G-2-550 composites before and after five cycles were depicted in Figure S7. EIS tests were performed at a status of open circuit voltage with frequency in between 10^5 to 0.01 Hz using as-assembled cells containing an electrode made of the samples. All these graphs display a hemicycle in the domain of high-middle frequency, corresponding to the resistance of charge transfer. At the same time, a straight line in the low-frequency zone representing the diffusion of Li^+ in these anode materials can also be observed in their EIS.[24] The inset in Figure S7 shows the equivalent circuit, in which R_Ω and R_{CT} represent the ohmic resistance (sum of resistance comes from electrolyte, separator, and electrical contacts) and the charge transfer resistance, respectively. CPE is the constant phase element and corresponds to the double layer capacitance, while W stands for the Warburg impedance, symbolizing the diffusion of Li ions into the bulk of active materials at a solid state.[61] In comparison with those of pure SnO_2 (∼148 Ω) and SnO_2/G-2-550 (∼102 Ω), the diameter of the semicircle in the EIS graph for SnO_2/G-1-550 (∼71 Ω) run for five turns is much smaller, reflecting a smaller charge transfer resistance (R_{CT}) in SnO_2/G-1-550 composite. Abnormally, diameter of semicircle in the EIS graph for the SnO_2/G-2-550 is even slightly larger than that of pristine SnO_2 sample before cycling owing to the bulk property of SnO_2/G-2-550 sample. After five cycles, the charge transfer resistance in SnO_2/G-2-550 sample became smaller in comparison with that of pristine SnO_2. Such a change is reasonable taking the existence of graphene and the porous structure of the SnO_2/G-2-550 sample into consideration. The graphene moiety integrated into a composite has been considered as essence for reducing the charge transfer resistance of the composite material. The aforementioned results confirmed the role of graphene in improving the electrochemical performances for an electrode consisting of SnO_2/G composite spheres.

4. CONCLUSIONS

In summary, unique 3D SnO_2/graphene composite spheres (SnO_2/G-1) with a skeleton structure have been induced through a simple spray-drying process. The framework of the skeleton is constructed with graphene sheets, in which the graphene layers were decorated by nanosized SnO_2 particles. In comparison with the pristine SnO_2 clusters and the SnO_2/graphene composite prepared via a normal evaporation method (SnO_2/G-2), the skeleton-structured SnO_2/G-1 samples exhibited significantly improved electrochemical performance as a lithium-ion battery anode and delivered a stable capacity of 1140 mA hg^{-1} after 120 cycles at a current density of 100 mA g^{-1}. Even at a high current density as high as 2000 mA g^{-1}, a capacity of 775 mAh g^{-1} could still be maintained after 50 cycles, showing an extraordinary rate capability performance. The remarkable electrochemical performance of SnO_2/G-1-550 is attributed to the synergistic effect between SnO_2 nano-

DOI: 10.1021/acsami.7b15916
ACS Appl. Mater. Interfaces 2018, 10, 2515−2525

particles and the graphene matrix. The skeleton-structured arrangements of the graphene sheets improve the surface area and pore volume of the composite spheres. The skeleton structure can act as a mechanical buffer to effectively alleviate the volume changes generated during the lithiation/delithiation processes. Such a skeleton structure is also beneficial to the transportation of electrolyte and the diffusion of lithium ions. Further development of this spray-drying-assisted method and their extension to other kinds of skeleton-structured graphene composites will make graphene-based composites more excellent as electrodes for high-performance LIBs or as electrodes of high-sensitivity sensors, and even as high-performance catalysts for photocatalytic reactions.

■ ASSOCIATED CONTENT

Supporting Information

The Supporting Information is available free of charge on the ACS Publications website at DOI: 10.1021/acsami.7b15916.

EDS elemental mapping analysis over a selected area in SnO_2/G-1-550; SEM images of SnO_2/GO-1-650 and SnO_2/GO-2-550 composites; TEM images and high-resolution TEM images of SnO_2/GO-1-650; TGA curve of the SnO_2/G-2-550 composite spheres; Nyquist plots of pristine SnO_2, SnO_2/G-1-550, and SnO_2/G-2 composites; a performance comparison of the SnO_2/G-1-550 sample with other documented SnO_2-based electrode materials for LIBs; SEM images of the SnO_2/G-1-550 electrode after repeated charge−discharge (PDF)

■ AUTHOR INFORMATION

Corresponding Author

*Tel: 0086-532-85950767; E-mail: lhl@qdu.edu.cn (H.L.)

ORCID

Yiqian Wang: 0000-0002-4135-6252

Yu-Guo Guo: 0000-0003-0322-8476

Peizhi Guo: 0000-0002-8773-2196

Author Contributions

The manuscript was written from contributions made by all authors. All authors have given approval to the final version of the manuscript.

Author Contributions

#D.L. and Z.K. contributed equally to this work.

Notes

The authors declare no competing financial interest.

■ ACKNOWLEDGMENTS

This work is supported by the Double First Class University Construction of Shandong Province, the Taishan Scholars Advantageous and Distinctive Discipline Program of Shandong Province for supporting the research team of energy storage materials, and Qingdao Basic & Applied Research Project (15-9-1-56-jch). Y.Q.W. thanks the financial support from the Top-notch Innovative Talent Program of Qingdao City (Grant no.: 13-CX-8).

■ REFERENCES

(1) Armand, M.; Tarascon, J. M. Building Better Batteries. *Nature* **2008**, *451*, 652−657.

(2) Whittingham, M. S. Lithium Batteries and Cathode Materials. *Chem. Rev.* **2004**, *104*, 4271−4302.

(3) Scrosati, B.; Garche, J. Lithium Batteries: Status, Prospects and Future. *J. Power Sources* **2010**, *195*, 2419−2430.

(4) Bruce, P. G.; Scrosati, B.; Tarascon, J. M. Nanomaterials for Rechargeable Lithium Batteries. *Angew. Chem., Int. Ed.* **2008**, *47*, 2930−2946.

(5) Kang, B.; Ceder, G. Battery Materials for Ultrafast Charging and Discharging. *Nature* **2009**, *458*, 190.

(6) Raccichini, R.; Varzi, A.; Passerini, S.; Scrosati, B. The Role of Graphene for Electrochemical Energy Storage. *Nat. Mater.* **2015**, *14*, 271−279.

(7) Jiang, C.; Hosono, E.; Zhou, H. Nanomaterials for Lithium Ion Batteries. *Nano Today* **2006**, *1*, 28−33.

(8) Etacheri, V.; Marom, R.; Elazari, R.; Salitra, G.; Aurbach, D. Challenges in the Development of Advanced Li-ion Batteries: a Review. *Energy Environ. Sci.* **2011**, *4*, 3243−3262.

(9) Manthiram, A. Materials Challenges and Opportunities of Lithium Ion Batteries. *J. Phys. Chem. Lett.* **2011**, *2*, 176−184.

(10) Zhang, W. A Review of the Electrochemical Performance of Alloy Anodes for Lithium-Ion Batteries. *J. Power Sources* **2011**, *196*, 13−24.

(11) Reddy, M.; Subba Rao, G. S.; Chowdari, B. Metal Oxides and Oxysalts as Anode Materials for Li Ion Batteries. *Chem. Rev.* **2013**, *113*, 5364−5457.

(12) Idota, Y.; Kubota, T.; Matsufuji, A.; Maekawa, Y.; Miyasaka, T. Tin-Based Amorphous Oxide: A High-Capacity Lithium-Ion-Storage Material. *Science* **1997**, *276*, 1395−1397.

(13) Kamali, A. R.; Fray, D. J. Tin-Based Materials as Advanced Anode Materials for Lithium Ion Batteries: A Review. *Rev. Adv. Mater. Sci.* **2011**, *27*, 14−24.

(14) Zhou, X. S.; Yu, L.; Lou, X. W. Formation of Uniform N-doped Carbon-Coated SnO_2 Submicroboxes with Enhanced Lithium Storage Properties. *Adv. Energy Mater.* **2016**, *6*, 1600451.

(15) Liang, J.; Zhao, Y.; Guo, L.; Li, L. Flexible Free-Standing Graphene/SnO_2 Nanocomposites Paper for LiIon Battery. *ACS Appl. Mater. Interfaces* **2012**, *4*, 5742.

(16) Xu, X.; Liang, J.; Zhou, H.; Lv, D. M.; Liang, F. X.; Yang, Z. L.; Ding, S. J.; Yu, D. M. The Preparation of Uniform SnO_2 Nanotubes with a Mesoporous Shell for Lithium Storage. *J. Mater. Chem. A* **2013**, *1*, 2995−2998.

(17) Liu, J.; Li, Y.; Huang, X.; Ding, R.; Hu, Y.; Jiang, J.; Liao, L. Direct Growth of SnO_2 Nanorod Array Electrodes for Lithium-Ion Batteries. *J. Mater. Chem.* **2009**, *19*, 1859−1864.

(18) Lin, Y.; Duh, J. G.; Hung, M. H. Shell-by-Shell Synthesis and Applications of Carbon-Coated SnO_2 Hollow Nanospheres in Lithium-Ion Battery. *J. Phys. Chem. C* **2010**, *114*, 13136−13141.

(19) Kong, J.; Liu, Z.; Yang, Z.; Tan, H.; Xiong, S.; Wong, S.; Li, X.; Lu, X. Carbon/SnO_2/Carbon Core/Shell/Shell Hybrid Nanofibers: Tailored Nanostructure for the Anode of Lithium Ion Batteries with High Reversibility and Rate Capacity. *Nanoscale* **2012**, *4*, 525−530.

(20) Cui, L.; Shen, J.; Cheng, F.; Tao, Z.; Chen, J. SnO_2 Nanoparticles@Polypyrrole Nanowires Composite as Anode Materials for Rechargeable Lithium-Ion Batteries. *J. Power Sources* **2011**, *196*, 2195−2201.

(21) Tu, F. Z.; Xu, X.; Wang, P. Z.; Si, L.; Zhou, X. S.; Bao, J. C. A Few-Layer SnS2/Reduced Graphene Oxide Sandwich Hybrid for Efficient Sodium Storage. *J. Phys. Chem. C* **2017**, *121*, 3261−3269.

(22) Zhou, X. S.; Yu, L.; Yu, X. Y.; Lou, X. W. Encapsulating Sn Nanoparticles in Amorphous Carbon Nanotubes for Enhanced Lithium Storage Properties. *Adv. Energy Mater.* **2016**, *6*, 1601177.

(23) Tang, Y.; Wu, D.; Chen, S.; Zhang, F.; Jia, J.; Feng, X. Highly Reversible and Ultra-fast Lithium Storage in Mesoporous Graphene-Based TiO_2/SnO_2 Hybrid Nanosheets. *Energy Environ. Sci.* **2013**, *6*, 2447−2451.

(24) Yang, S.; Yue, W. B.; Zhu, J.; Ren, Y.; Yang, X. J. Graphene-Based Mesoporous SnO_2 with Enhanced Electrochemical Performance for Lithium-Ion Batteries. *Adv. Funct. Mater.* **2013**, *23*, 3570−3576.

(25) Zhou, X. S.; Yin, Y. X.; Wan, L. J.; Guo, Y. G. A Robust Composite of SnO_2 Hollow Nanospheres Enwrapped by Graphene as

a High-Capacity Anode Material for Lithium-Ion Batteries. *J. Mater. Chem.* **2012**, *22*, 17456−17459.
(26) Zhang, W. M.; Hu, J. S.; Guo, Y. G.; Zheng, S. F.; Zhong, L. S.; Song, W. G.; Wan, L. J. Tin-Nanoparticles Encapsulated in Elastic Hollow Carbon Spheres for High-Performance Anode Material in Lithium-Ion Batteries. *Adv. Mater.* **2008**, *20*, 1160−1165.
(27) Jing, L. Y.; Fu, A. P.; Li, H. L.; Liu, J. Q.; Guo, P. Z.; Wang, Y. Q.; Zhao, X. S. One-Step Solvothermal Preparation of Fe_3O_4/Graphene Composites at Elevated Temperature and Their Application as Anode Materials for Lithium-Ion Batteries. *RSC Adv.* **2014**, *4*, 59981−59989.
(28) Prabakar, S. J. R.; Hwang, Y. H.; Bae, E. G.; Shim, S. D.; Kim, D. W.; Lah, M. S.; Sohn, K. S.; Pyo, M. SnO_2/Graphene Composites with Self-Assembled Alternating Oxide and Amine Layers for High Li-Storage and Excellent Stability. *Adv. Mater.* **2013**, *25*, 3307−3312.
(29) Zhou, X. S.; Wan, L. J.; Guo, Y. G. Binding SnO_2 Nanocrystals in Nitrogen-Doped Graphene Sheets as Anode Materials for Lithium-Ion Batteries. *Adv. Mater.* **2013**, *25*, 2152−2157.
(30) Zhang, X.; Liang, J.; Gao, G.; Ding, S.; Yang, Z.; Yu, W.; Li, B. The Preparation of Mesoporous SnO_2 Nanotubes by Carbon Nanofibers Template and Their Lithium Storage Properties. Electrochim. *Electrochim. Acta* **2013**, *98*, 263−267.
(31) Kim, W. S.; Hwa, Y.; Jeun, J. H.; Sohn, H. J.; Hong, S. H. Synthesis of SnO_2 Nano Hollow Spheres and Their Size Effects in Lithium Ion Battery Anode Application. *J. Power Sources* **2013**, *225*, 108−112.
(32) Wang, Z.; Luan, D.; Boey, F. Y. C.; Lou, X. Fast Formation of SnO_2 Nanoboxes with Enhanced Lithium Storage Capability. *J. Am. Chem. Soc.* **2011**, *133*, 4738−4741.
(33) Wu, Z.; Zhou, G.; Yin, L.; Ren, W.; Li, F.; Cheng, H. Graphene/Metal Oxide Composite Electrode Materials for Energy Storage. *Nano Energy* **2012**, *1*, 107−131.
(34) Lin, J.; Peng, Z.; Xiang, C.; Ruan, G.; Yan, Z.; Natelson, D.; Tour, J. M. Graphene Nanoribbon and Nanostructured SnO_2 Composite Anodes for Lithium Ion Batteries. *ACS Nano* **2013**, *7*, 6001−6006.
(35) Han, S.; Wu, D. Q.; Li, S.; Zhang, F.; Feng, X. L. Porous Graphene Materials for Advanced Electrochemical Energy Storage and Conversion Devices. *Adv. Mater.* **2014**, *26*, 849−864.
(36) Li, Y.; Lv, X.; Lu, J.; Li, J. Preparation of SnO_2-Nanocrystal/Graphene-Nanosheets Composites and Their Lithium Storage Ability. *J. Phys. Chem. C* **2010**, *114*, 21770−21774.
(37) Li, F.; Song, J.; Yang, H.; Gan, S.; Zhang, Q.; Han, D.; Ivaska, A.; Niu, L. One-Step Synthesis of Graphene/SnO_2 Nanocomposites and Its Application in Electrochemical Supercapacitors. *Nanotechnology* **2009**, *20*, 455602.
(38) Zhao, K. N.; Zhang, L.; Xia, R.; Dong, Y. F.; Xu, W. W.; Niu, C. J.; He, L.; Yan, M.; Qu, L.; Mai, L. SnO_2 Quantum Dots@Graphene Oxide as a High-Rate and Long-Life Anode Material for Lithium-Ion Batteries. *Small* **2016**, *12*, 588−594.
(39) Liu, X. W.; Cheng, J. X.; Li, W. H.; Zhong, X. W.; Yang, Z. Z.; Gu, L.; Yu, Y. Superior Lithium Storage in a 3D Macroporous Graphene Framework/SnO_2 Nanocomposite. *Nanoscale* **2014**, *6*, 7817−7822.
(40) Zhao, B.; Xu, Y. T.; Huang, S. Y.; Zhang, K.; Yuen, M. M. F.; Xu, J. B.; Fu, X. Z.; Sun, R.; Wong, C. P. 3D RGO Frameworks Wrapped Hollow Spherical SnO_2-Fe_2O_3 Mesoporous Nano-Shells: Fabrication, Characterization and Lithium Storage Properties. *Electrochim. Acta* **2016**, *202*, 186−196.
(41) Shen, R. X.; Hong, Y. Z.; Stankovich, J. J.; Wang, Z. Y.; Dai, S.; Jin, X. B. Synthesis of Cambered Nano-walls of SnO_2/rGO Composites Using a Recyclable Melamine Template for Lithium-Ion Batteries. *J. Mater. Chem. A* **2015**, *3*, 17635−17643.
(42) Lou, X. W.; Wang, Y.; Yuan, C. L.; Lee, J. Y.; Archer, L. A. Template-Free Synthesisof SnO_2 Hollow Nanostructureswith High Lithium Storage Capacity. *Adv. Mater.* **2006**, *18*, 2325−2329.
(43) Yu, Y.; Gu, L.; Wang, C. L.; Dhanabalan, A.; van Aken, P. A.; Maier, J. Encapsulation of Sn@Carbon Nanoparticles in Bamboo-like Hollow Carbon Nanofibers as an Anode Material in Lithium-Based Batteries. *Angew. Chem., Int. Ed.* **2009**, *48*, 6485−6489.
(44) Zhang, j.; Li, M.; Feng, C.; Chen, J.; Li, C. UV Raman Spectroscopic Study on TiO_2. I. Phase Transformation at the Surface and in the Bulk. *J. Phys. Chem. B* **2006**, *110*, 927−935.
(45) Okada, K.; Yamamoto, N.; Kameshima, Y.; Yasumori, A.; MacKenzie, K. J. D. Effect of Silica Additive on the Anatase-to-Rutile Phase Transition. *J. Am. Ceram. Soc.* **2001**, *84*, 1591−1596.
(46) Lian, P.; Zhu, X.; Xiang, H.; Li, Z.; Yang, W.; Wang, H. Enhanced Cycling Performance of Fe_3O_4-Graphene Nanocomposite as an Anode Material for Lithium-Ion Batteries. Electrochim. *Electrochim. Acta* **2010**, *56*, 834−840.
(47) Li, H. L.; Liu, H.; Fu, A. P.; Wu, G. L.; Xu, M.; Pang, G. S.; Guo, P. Z.; Liu, J. Q.; Zhao, X. S. Synthesis and Characterization of N-Doped Porous TiO_2 Hollow Spheres and Their Photocatalytic and Optical Properties. *Materials* **2016**, *9*, 849.
(48) Yang, S.; Yue, W. B.; Huang, D.; Chen, C.; Lin, H.; Yang, X. A Facile Green Strategy for Rapid Reduction of Graphene Oxide by Metallic Zinc. *RSC Adv.* **2012**, *2*, 8827−8832.
(49) Zhang, L.; Zhao, K. N.; Yu, R. H.; Yan, M. Y.; Xu, W. W.; Dong, Y. F.; Ren, W. H.; Xu, X.; Tang, C.; Mai, L. Q. Phosphorus Enhanced Intermolecular Interactions of SnO_2 and Graphene as an Ultrastable Lithium Battery Anode. *Small* **2017**, *13*, 1603973.
(50) Wang, Q.; Fu, A. P.; Li, H. L.; Liu, J. Q.; Guo, P. Z.; Zhao, X. S.; Xia, L. H. Preparation of Cellulose Based Microspheres by Combining Spray Coagulating with Spray Drying. *Carbohydr. Polym.* **2014**, *111*, 393−399.
(51) Li, H. L.; Sang, J. J.; Zhao, J. H.; Fu, A. P.; Liu, H.; Xu, M.; Pang, G. S.; Zhao, X. S. Preparation of Magnetically Separable Mesoporous Co@Carbon/Silica Composites by the RAPET Method. *New J. Chem.* **2012**, *36*, 2308−2315.
(52) Li, F. H.; Song, J. F.; Yang, H. F.; Gan, S. Y.; Zhang, Q. X.; Han, D. X.; Ivaska, A.; Niu, L. One-Step Synthesis of Graphene/SnO_2 Nanocomposites and Its Application in Electrochemical Supercapacitors. *Nanotechnology* **2009**, *20*, 455602.
(53) Wang, D. X.; Fu, A. P.; Li, H. L.; Wang, Y. Q.; Liu, J. Q.; Guo, P. Z.; Zhao, X. S. Mesoporous Carbon Spheres with Controlled Porosity for High-Performance Lithium-Sulfur Batteries. *J. Power Sources* **2015**, *285*, 469−477.
(54) Ko, Y. D.; Kang, J. G.; Park, J. G.; Lee, S. J.; Kim, D. W. Self-Supported SnO_2 Nanowire Electrodes for High-Power Lithium-Ion Batteries. *Nanotechnology* **2009**, *20*, 455701.
(55) Zhou, H. S.; Zhu, S. M.; Hibino, M.; Honma, I.; Ichihara, M. Lithium Storage in Ordered Mesoporous Carbon (CMK-3) with High Reversible Specific Energy Capacity and Good Cycling Performance. *Adv. Mater.* **2003**, *15*, 2107−2111.
(56) Zhao, X. W.; Zhang, J. W.; Zhang, J. W.; Gong, C. H.; Gu, X. F.; Ma, Z. H.; Zhou, J. F.; Yu, L. G.; Zhang, Z. J. Construction of Spongy Antimony-Doped Tin Oxide/Graphene Nanocomposites Using Commercially Available Products and Its Excellent Electrochemical Performance. *J. Power Sources* **2015**, *294*, 223−231.
(57) Li, W. Y.; Yoon, D.; Hwang, J.; Chang, W.; Kim, J. One-Pot Route to Synthesize SnO_2-Reduced Graphene Oxide Composites and Their Enhanced Electrochemical Performance as Anodes in Lithium-ion Batteries. *J. Power Sources* **2015**, *293*, 1024−1031.
(58) Ma, Y.; Asfaw, H. D.; Edström, K. Three-Dimensional Carbon Foam Supported Tin Oxide Nanocrystallites with Tunable Size Range: Sulfonate Anchoring Synthesis and High Rate Lithium Storage Properties. *J. Power Sources* **2015**, *294*, 208−215.
(59) Deng, Y.; Fang, C.; Chen, G. The Developments of SnO_2/Graphene Nanocomposites as Anode Materials for High Performance Lithium Ion Batteries: A Review. *J. Power Sources* **2016**, *304*, 81−101.
(60) Liang, J.; Yu, X. Y.; Zhou, H.; Wu, H. B.; Ding, S. J.; Lou, X. W. Bowl-Like SnO_2@Carbon Hollow Particles as an Advanced Anode Material for Lithium-Ion Batteries. *Angew. Chem., Int. Ed.* **2014**, *53*, 12803−12807.
(61) Reddy, M. V.; Subba Rao, G. V.; Chowdari, B. V. R. Long-Term Cycling Studies on 4 V-Cathode, Lithium Vanadium Fluorophosphate. *J. Power Sources* **2010**, *195*, 5768−5774.

DOI: 10.1021/acsami.7b15916
ACS Appl. Mater. Interfaces 2018, 10, 2515−2525